

A Highly Stretchable and Sensitive Strain Sensor Based on Dopamine Modified Electrospun SEBS Fibers and MWCNTs with Carboxylation

Bangze Zhou ¹, Zhanxu Liu ¹, Chenchen Li ¹, Mengsi Liu ¹, Liang Jiang ^{1,2,*}, Yanfen
Zhou ^{1,2,*}, Fenglei Zhou ^{1,3}, Shaojuan Chen ^{1,2}, Stephen Jerrams ⁴, Jianyong Yu ⁵

¹ College of Textiles and Clothing, Qingdao University, Qingdao 266071, China

² Eco-Textile Collaborative Innovation Center, Qingdao University, Qingdao, 266071,
China

³ Centre for Medical Image Computing, University College London, London, WC1V
6LJ, UK

⁴ Centre for Elastomer Research, Focas Research Institute, Technological University
Dublin (TUD), City Campus, Kevin St, Dublin D08 NF82, Ireland

⁵ Innovation Center for Textile Science and Technology, Donghua University,
Shanghai 200051, China

* Corresponding author, email address: liang.jiang@qdu.edu.cn

* Corresponding author, email address: yanfen.zhou@qdu.edu.cn

Abstract

Wearable flexible electronic strain sensor devices have developed rapidly in recent years due to their potential capacity to detect human motion in various situations. However, it still remains still a big challenge to fabricate strain sensors with high sensitivity over a wide workable strain range. In order to meet this challenge, a new type of strain sensor based on elastomer/carbon nanotube composite fiber was reported in this work. Elastomer fibers were initially prepared via the electrospinning of styrene ethylene butene styrene block copolymer (SEBS). The resultant SEBS fibers were then functionalized by sequentially coating with dopamine (DA) coating and carboxyl group (-COOH) grafted multi-walled carbon nanotubes (MWCNTs) under vacuum filtration and ultrasonication. Scanning electron microcopy (SEM) and **thermogravimetric (TG) analysis** revealed that a large amount of MWCNTs were firmly bonded onto the SEBS fibers and evenly distributed. SEBS@PDA/MWCNTs composite fibers based strain sensors exhibited excellent performance, including a high gauge factor of 3717, a large workable strain range up to 530%. Furthermore, the developed sensors demonstrated excellent washing fastness and superior sensitivity in monitoring both small strains (e.g. pulse beats and vocal cord vibrations) and large strains (e.g. finger, elbow and knee bending).

Key words: SEBS, dopamine, MWCNTs, sensor

1. Introduction

Wearable flexible electronic strain sensor devices have been undergoing rapid development. They have been proposed to detect various human physiological activities including the large motion of hands, arms and legs, as well as smaller motions of breathing, swallowing, vocal cord vibration, blood pressure, etc. [1,2], with the benefit of converting mechanical deformations into electrical signals including capacitance and resistance. Traditional strain sensors, which are mainly based on semiconductors and metals, suffer fragility, poor extensibility and unstable conductivity and therefore cannot meet the requirement of flexible strain sensor [3]. So far, flexible strain sensors have been fabricated by using low-dimensional carbon materials and flexible matrix materials. Low-dimensional carbon materials are used as conductive materials, such as carbon nanotubes (CNTs), carbon blacks (CBs), graphene [3-5], nanowires (NWs) [6,7], nanoparticles (NPs) [8,9] and their hybrid micro/nanostructures [10,11], while flexible matrix materials of strain sensors are elastic polymers including thermoplastic polyurethane (TPU) [7,8,12], styrene-butadiene-styrene block copolymer (SBS) [3,13], styrene-ethylene-butene-styrene block copolymer (SEBS) [10,14], polydimethylsiloxane (PDMS) [4,15], Ecoflex [16] and others.

Currently, there are numerous methods to prepare strain sensors by combining conductive nano-materials with elastomers. However, most sensors cannot simultaneously possess high sensitivity and high workable strain. This sensitivity is given by the gauge factor (GF):

$$GF = (\Delta R/R_0)/\varepsilon \quad (1)$$

where $\Delta R = R - R_0$, R represents real-time resistance changes, R_0 represents the initial

resistance of strain sensors and ε is the applied strain. High extensibility is indicated by high values of strain, ε . For example, Lee et al. [17] fabricated a highly sensitive pressure and strain sensor by depositing a cracked transparent epilayer, **indium-tin oxide** on a transparent **polyethylene terephthalate** substrate, which had a high GF of 4000 at a maximum workable strain of 2%. Wang et al. [18] reported a stretchable strain sensor fabricated by incorporating single-wall carbon nanotubes (SWCNTs) into an elastic cotton/**TPU** core-spun yarn via a self-designed coating approach, which had a workable strain of 200%, but with a very low GF of only 0.06. Sang et al. [6] developed a sensitive strain sensor based on silver nanowires and nanoparticles containing PDMS, which possessed a high GF of 3766 but a low workable strain of just 28.1%. Ren et al. [19] reported a CNTs/TPU composite based strain sensor that could be stretched up to 900%, though its GF was only 20. Therefore, there is a great impetus to develop a facile method that can fabricate a polymer-based strain sensor with both high extensibility and high sensitivity.

SEBS is a thermoplastic elastomer, possessing excellent tensile properties and elastic recovery properties. It has been widely used as the matrix for fabricating stretchable conductive materials, flexible shielding materials and stretchable corrosion-resistant materials [20-23]. However, its low surface energy and polarity result in poor compatibility and weak adhesion to inorganic materials, thus it often requires modification prior to use [24]. Dopamine (DA) is a kind of nontoxic and environmentally friendly material. Because it contains catechol and amino groups, it can self polymerize into polydopamine (PDA), which is similar to the mucin secreted

by mussels and has strong adhesion properties [25].

In the present study, **multi-walled carbon nanotubes (MWCNTs)** were adapted for the fabrication of strain sensors because MWCNTs have high mechanical strength and excellent electrical properties. In order to minimize the agglomeration of MWCNTs caused by their strong van der Waals force and improve their dispersion in the matrices, a carboxyl group was introduced to the surface of MWCNTs through chemical methods. Then, an easy and practical approach to fabricating SEBS@PDA/MWCNTs composite fibers based strain sensor was reported. Firstly, SEBS fibers were fabricated via the technique of electrospinning, which can process fibers with huge surface-area-to-volume ratio, high porosity, and tunable inner structures [26]. Then PDA was used to modify the surface of the electrospun SEBS fibers, followed by coating MWCNTs-COOH. The morphology and electrical property of SEBS@PDA/MWCNTs composite fibers were investigated via Scanning electron microscopy (SEM), Energy-dispersive X-ray spectroscopy (EDX), and a multifunctional digital four-probe tester. Thirdly, mechanical properties were tested by a universal testing machine, and the composite fibers exhibited outstanding extensibility, flexibility and mechanical strength. Fourthly, the extensibility, electromechanical stability and wash fastness were also evaluated. Finally, the sensing performance of SEBS@PDA/MWCNTs composite fibers were demonstrated by detecting various human large motions (such as at fingers, knuckles and wrists) and subtle motions in physiological activities, involved in speaking and pulse beat.

2. Experiment

2.1. Materials

SEBS G1651H (EP/PS = 67/33 wt.%) was supplied by the Kraton Corporation, USA. Tetrahydrofuran (THF), hydrochloric acid (HCl), **nitric acid (HNO₃)**, **sulphuric acid (H₂SO₄)** and absolute alcohol were purchased from Sinopharm Chemical Reagent Co., Ltd, China. Dopamine hydrochloride (DA/HCl) and sodium periodate (SP) were supplied by Shanghai Macklin Biochemical Co., Ltd, China. Tris(hydroxymethyl)methyl aminomethane (Tris) was supplied by Beijing Solarbio Science & Technology Co., Ltd, China. MWCNTs were purchased from Shenzhen Tuling Evolution Technology Co., Ltd, China.

2.2. Preparation of composite fibers based strain sensor

The full procedure, depicted in Figure 1, involves 5 steps: (1) electrospinning SEBS fibers; (2) DA modification; (3) MWCNTs-COOH coating; (4) ultrasonication; (5) drying.

2.2.1. Electrospinning of SEBS fibers

SEBS and THF were mixed with a SEBS concentration of 25 wt.% for 12 h. Then the solution was loaded into a 20 ml syringe connected to a 22 G needle, and fixed onto a syringe pump. The whole electrospinning process was carried out at a temperature of 20 ~ 25 °C, humidity of 30 ~ 40%, applied voltage of 10 kV, solution injection speed of 3 mL/h, rotational speed of drum collector of 100 rev/min and working distance of 15 cm between the needle tip and the collector for 4 h. Finally, the electrospun SEBS fibers were placed in a fume hood overnight at room temperature.

2.2.2. Dopamine modification of electrospun SEBS fibers

For the surface modification of SEBS fibers, a 10 mmol/L DA solution was prepared by dissolving DA/HCl powder into Tris-HCl solution (pH = 8.5). Then SP was added into this DA solution to form the mixed solution with a mole ratio of DA and SP of 3:2. Subsequently, SEBS fibers were soaked in a DA/SP solution for 2 h and were washed afterward with distilled water and dried at 70 °C in an oven. The resulting material was herein denoted as SEBS@PDA.

2.2.3. Preparation of MWCNTs-COOH

MWCNTs were treated with ultrasonication for 12 h in H₂SO₄/HNO₃ (3:1) mixed acid with a concentration of 10 g/L, followed by stirring for 8 h at 65 °C. The mixture of MWCNTs-COOH was centrifuged at 6000 r/min for 20 min, filtered through 0.22 μm filter paper, washed to neutral with distilled water and dried in a vacuum at 40 °C. Detailed description of MWCNTs and MWCNTs-COOH characterization was presented in Supporting Information.

2.2.4. Preparation of MWCNTs-coated composite fibers

Firstly, MWCNTs-COOH suspension was prepared by mixing MWCNTs-COOH and absolute alcohol with a concentration of 1 g/L. Then MWCNTs were coated onto the SEBS and SEBS@PDA fibers by vacuum filtration at different time intervals, 50 mL MWCNTs suspension was filtrated at each time. After vacuum filtration, MWCNT-coated fibers were soaked in distilled water under ultrasonication working at 240 W and 50 kHz at 25 °C for 5 min to remove MWCNTs with weak adhesion and dried at 60 °C in an oven. The composite fibers obtained were denoted as SEBS@PDA/xMWCNTs

in which x represented the times of vacuum filtration.

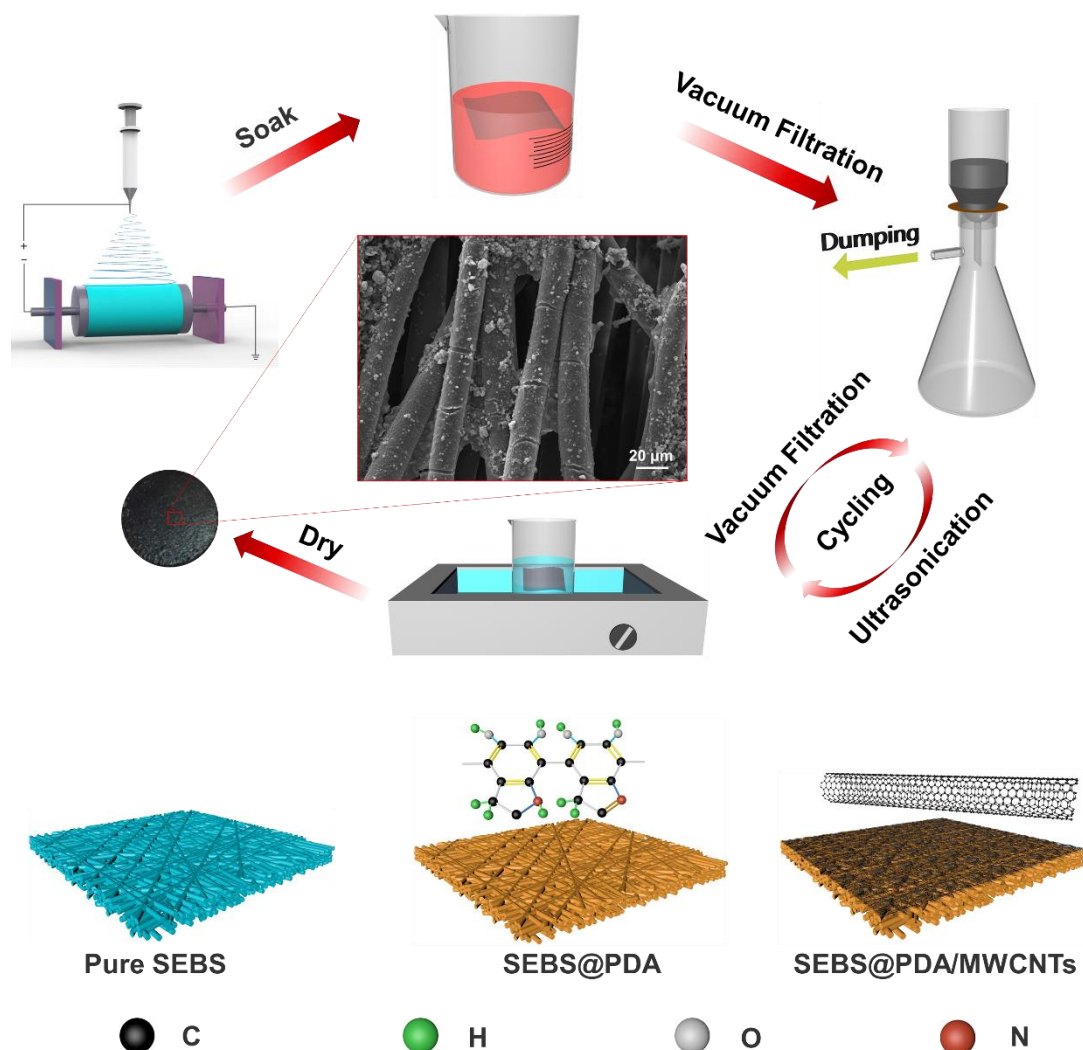


Figure 1 Illustrations of fabricating SEBS@PDA/MWCNTs fiber composite

2.5 Microstructural, mechanical and electrochemical Characterization

Scanning electron microscope (SEM, TESCAN VEGA3, Czech) was applied to observe the morphology of the electrospun fibers. The surface of samples was sputtered with gold layers before observation and SEM images with different magnifications were captured at an accelerated voltage of 10 kV.

Energy-dispersive X-ray spectroscopy (EDX, EDAXTM, US), was applied to characterize elemental composition and distribution on the surface of fibers.

A multifunctional digital four-probe tester (ST-2258C, Suzhou Jingge Electronics, China) was used to measure the sheet resistance of samples. The final data point of sheet resistance was the average of the results obtained from tests on 3 samples under the same condition.

A universal testing machine (Instron 3300, Glenview, USA) was used to test mechanical properties under standard conditions (25 °C/65% RH) with the uniaxial tensile force applied at a stretching speed of 100 mm/min. The size of each sample was 10 mm in width and 20 mm in length.

The surface chemical structure was determined using Fourier transform infrared spectroscopy (FTIR) (Nicolet 5700, Massachusetts, USA). The spectrum was collected in the wavenumber range from 4000 cm^{-1} to 400 cm^{-1} at scanning times of 32 and resolution of 4 cm^{-1} .

The surface chemical composition of the fibers was determined by X-ray photoelectron spectroscopy (XPS, Axis Supra⁺, Kratos, Japan). An Al $K\alpha$, the X-ray was used at 15 kV and 10 mA, and the C1s peak is shifted to 284.8 eV for energy calibration.

A DSC/TG synchronous thermal analyzer (STA449 F3 Jupiter, Bavaria, Germany) was used to do thermogravimetric analysis. The test was carried out in a nitrogen atmosphere. The sample, with a weight of about 5 mg, was heated from ambient temperature to 800 °C with a heating rate of 20 °C/min.

Electromechanical properties of fibers were tested by employing a digital multimeter (KEYSIGHTB2901A, Keysight Technology, USA) which was equipped with a stepper motor to induce various tensile deformations to the samples.

3. Results and discussion

3.1 Microstructural and physical characterization

Figure 2 shows the SEM images and EDX mapping of pure SEBS fibers and SEBS@PDA fibers. It can be seen from Figure 2a and b that the surface of the SEBS fibers was smooth with an absence of deposited particles while the surface of SEBS@PDA fibers was roughened by the presence of PDA. EDX spectrum images and mapping images in Figure 2a', 3b' and 2c-e show the presence and distribution of nitrogen and oxygen elements on the SEBS@PDA fibers, confirming the successful deposition of DA on SEBS fibers.

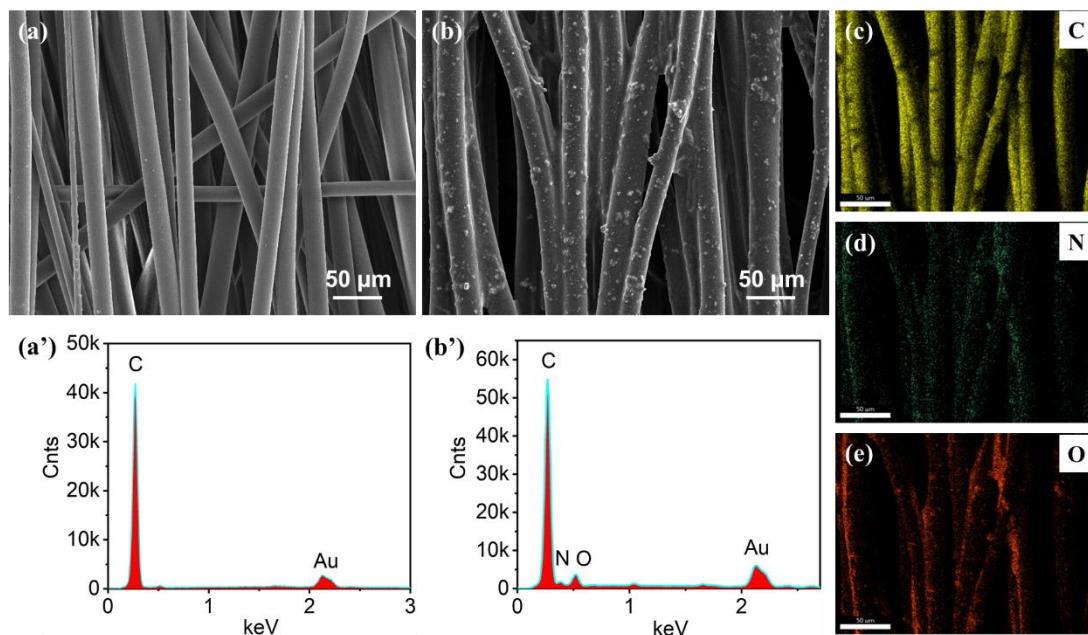


Figure 2 SEM images and EDX spectroscopy of (a), (a') pure SEBS and (b), (b') SEBS@PDA, respectively. EDX mapping images of SEBS@PDA for (c) C, (d) N, and (e) O.

Thermogravimetric (TG) analysis was employed to quantify the amount of MWCNTs

coated on SEBS fibers with varying vacuum filtration times. Figure 3 shows the TG curves of SEBS based fibers used in this work. As shown in Figure 3a and 4b, the weight loss of fibers decreased with increasing vacuum filtration times in a temperature range of 40 °C to 800 °C. When the temperature reached 800 °C, the weight loss of pure SEBS fibers and MWCNTs-coated SEBS fibers with increasing vacuum filtration times were 2.15%, 5.42%, 9.06%, 13.04%, 18.02% and 20.5% respectively, and the weight loss of SEBS@PDA fibers, MWCNTs-coated SEBS@PDA fibers with increasing vacuum filtration times were 3.89%, 7.82%, 12.53%, 15.61%, 23.04% and 28.42% respectively. Figure 3c shows the relation between the content of MWCNT on fiber surface and the vacuum filtration times. It can be seen that the deposition content of MWCNTs increased with increasing the vacuum filtration times for SEBS fibers with and without DA. For the SEBS fibers without DA modification, the MWCNTs content was approximately 3.27% after one vacuum filtration, while the content reached 18.35% after five times vacuum filtration cycles. For the SEBS fibers with DA modification, the MWCNTs content was about 3.93% for a single vacuum filtration while it was up to 24.53% after it had undergone five times vacuum filtration cycles. As shown in **Figure 3c**, the MWCNTs content of SEBS@PDA/MWCNTs composite fibers was 7.84 ~ 32% higher than that of SEBS/MWCNTs composites after undergoing the same numbers of vacuum filtration. It is assumed that the attraction between the ion on amide group on DA and polyanion contained in carboxyl group attributed to a higher deposition of MWCNTs [27].

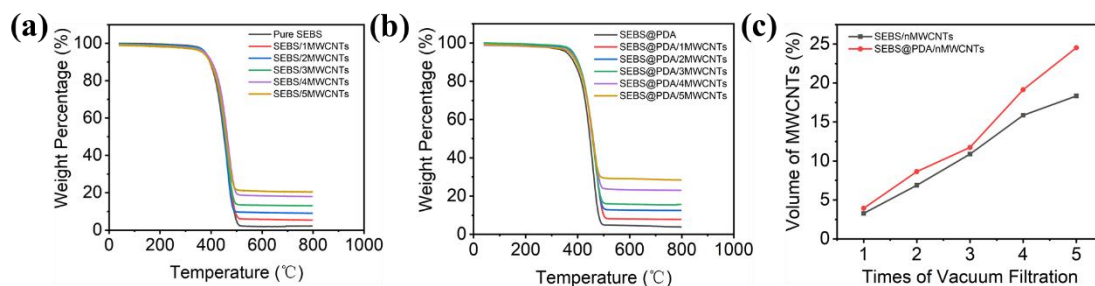


Figure 3 TGA curves of (a) SEBS/MWCNTs and (b) SEBS@PDA/MWCNTs after undergoing different times of vacuum filtration. (c) the relation between the MWCNTs content of SEBS/MWCNTs fibers and SEBS@PDA/MWCNTs fibers after undergoing different times of vacuum filtration.

3.2 Chemical structure characterization

Figure 4 provides the XPS spectra of pure SEBS, SEBS@PDA and SEBS@PDA/MWCNTs composite fibers. As shown in Figure 4a, the binding energy of 284.8 eV of pure SEBS was assigned to the carbon skeleton, while the presence of oxygen peak at 532 eV of pure SEBS was due to the air pollution. Compared with pure SEBS, a new peak of N1s at 399 eV appeared in the spectra of SEBS@PDA and SEBS@PDA/MWCNTs fibers, indicating successful modification of DA on SEBS fibers.

As shown in Figure 4b, a C-C peak at 284.8 eV and π - π^* satellite peak at 291.5 eV, C-O peak at 286 eV also appeared owing to the air pollution. After DA modification, there was a new peak at 285.5 eV, indicating the formation of C-N (Figure 4c). After the MWCNTs-COOH were coated, the observation of sp^2 C peak at 284 eV and O-C=O peak at 289 eV, as shown in Figure 4d, proved that PDA and MWCNTs were coated onto SEBS fibers.

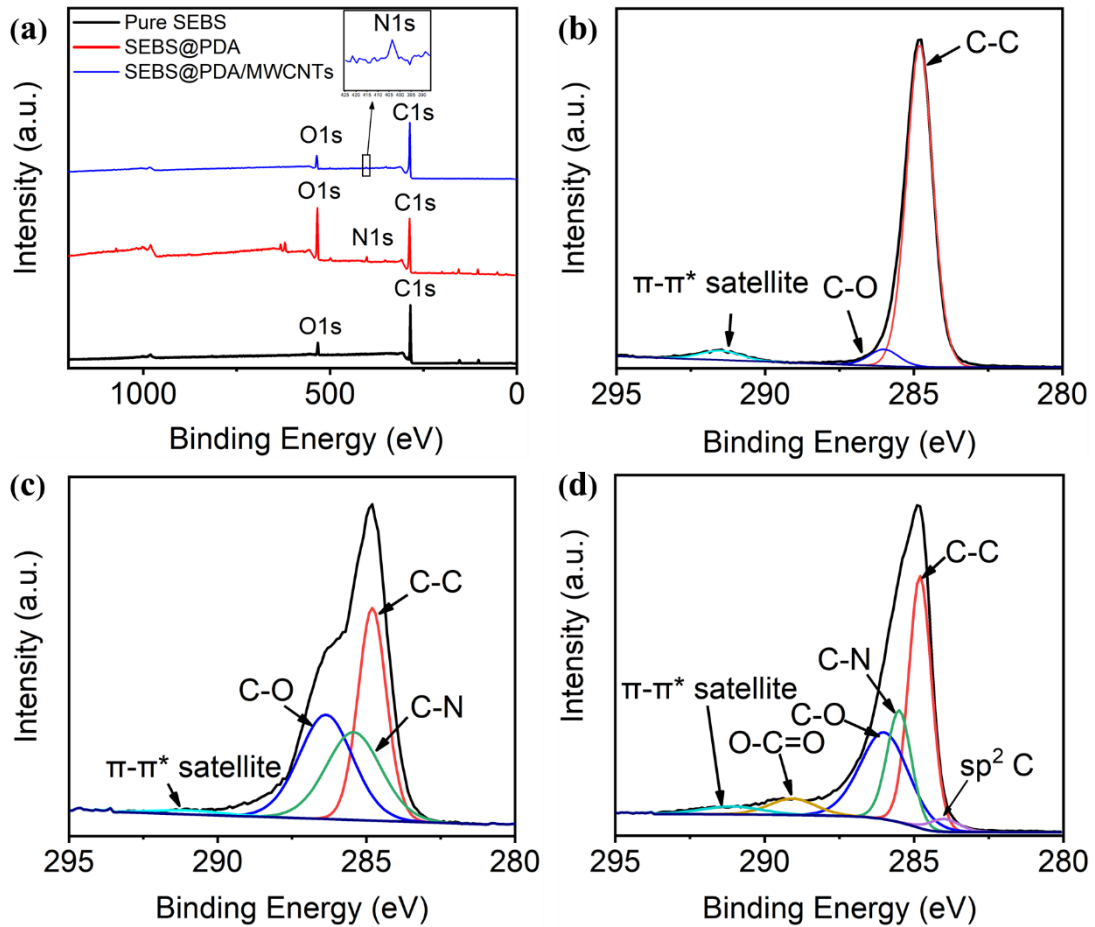


Figure 4 (a) XPS wide scan spectra of pure SEBS, SEBS@PDA and SEBS@PDA/MWCNTs. C1s core-level spectra of (b) pure SEBS, (c) SEBS@PDA, (d) SEBS@PDA/MWCNTs.

3.3 Electrical property

Figure 5 illustrates the change in sheet resistance of composite fiber with increasing time of vacuum filtration and SEM images of the corresponding composite fibers. As shown in Figure 5a, with a single vacuum filtration, composite fibers were not electrically conductive. However, after a 2nd vacuum filtration, the composite fibers had the sheet resistance of 5.72 ± 5.6 k Ω /sq. Interestingly, between the 4th and 5th vacuum filtration, there was nearly no change in the sheet resistance of the composite fibers, 1.34 ± 0.24 vs 1.33 ± 0.42 k Ω /sq. This can be explained by the percolation theory [28,29]

which is related to a critical concentration of conductive fillers in polymer composites. This critical concentration of filler is termed the percolation threshold. In the region of percolation threshold, the formation of the continuous conducting network merely occurs through filler arrangements in the polymer matrix. Above the percolation threshold, the resistance decreases slightly and tends to gradually stabilize with the formation of conducting networks. Based on this consideration, 4 vacuum filtration times was used to deposit MWCNTs layer on SEBS fibers.

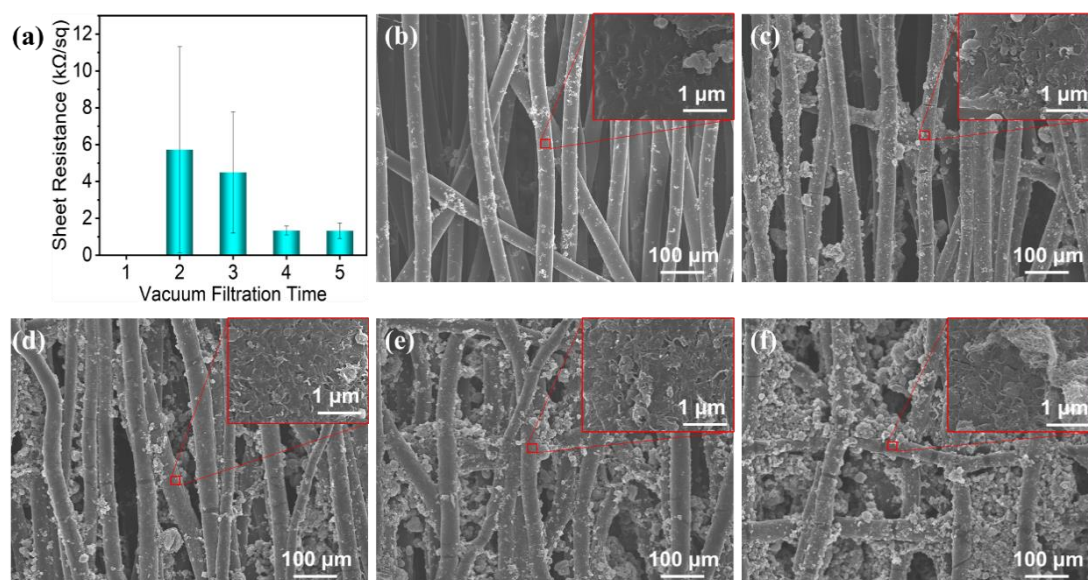


Figure 5 (a) Sheet resistance of fiber composite. SEM images of (b) SEBS@PDA/1MWCNTs, (c) SEBS@PDA/2MWCNTs, (d) SEBS@PDA/3MWCNTs, (e) SEBS@PDA/4MWCNTs, and (f) SEBS@PDA/5MWCNTs

3.4 Mechanical properties

It is generally known that providing appropriate, mechanical properties of materials is essential for practical applications [30]. Figure 6a shows typical stress–strain curves of pure SEBS, SEBS@PDA and SEBS@PDA/MWCNTs fibers. The corresponding

tensile strength, elongation at break and elastic modulus for each material were summarized in Table 1. The pure SEBS fibers had a tensile strength of 1.84 MPa and an elastic modulus of 8.33 MPa respectively. With the deposition of both PDA and MWCNTs, the tensile strength and elastic modulus of SEBS fibers increased. SEBS@PDA fibers had a tensile strength of 2.01 MPa and elastic modulus of 10.98 MPa while SEBS@PDA/MWCNTs fibers had a tensile strength of 2.39 MPa and elastic modulus of 11.67 MPa. This trend was primarily as a result of the PDA layer acting as a glue-like adhesive, making the fibers adhere strongly to each other and to MWCNTs coating. The formation of strong interface between MWCNTs and fibers effectively transferred the stress from fibers to MWCNTs contributed to an enhancement of mechanical properties [31,32]. However, the elongation at break of SEBS@PDA and SEBS@PDA/MWCNTs decreased to 683.05% and 626.92% respectively, compared with that of pure SEBS fibers (929.3%). The agglomerates of PDA and MWCNTs led to local stress concentrations and promote early fracture [33]. Mechanical hysteresis also plays a critical role in the performance of a strain sensor [34]. To investigate the relationship between the viscoelastic behavior and reproducibility of strain sensor performance, cyclic tensile testing under applied strains of 50%, 100% and 250% at a stretching rate of 100 mm/min were carried out. As shown in Figure 6b-d, as with all cyclic loading, the unloading curves did not follow the loading curves in each cycle, leading to the formation of hysteresis loops with different sizes and shapes.

Dissipated energy [33] characterized mechanical hysteresis and was calculated from

the area of the hysteresis loop in each cycle. Figure 6e shows the dissipated energy of SEBS, SEBS@PDA and SEBS@PDA/MWCNTs fibers at different strains in 5 cycles. The dissipated energy increased with the increasing tensile strains and the deposition of both PDA and MWCNTs, reflecting that the higher tensile strengths and elastic moduli were achieved after PDA and/or MWCNTs coating. Also, the dissipated energy was the highest in the first cycle, and then tended toward a constant value in subsequent cycles for each type of sample. This observation was consistent with greater stress softening in early cycles for all elastomeric materials (Mullins Effect) [35]. According to the reported literature [3], mechanical hysteresis was generated from irreversible deformation due to the slippage between PDA, MWCNTs and SEBS fibers, and between the chain segments of SEBS. During the first stretch, unstable contact and internal bonds broke irreversibly and did not reform during the release, especially as the applied strain increased [36]. Thus, in the following cycles lower forces were required to reach the initial elongation.

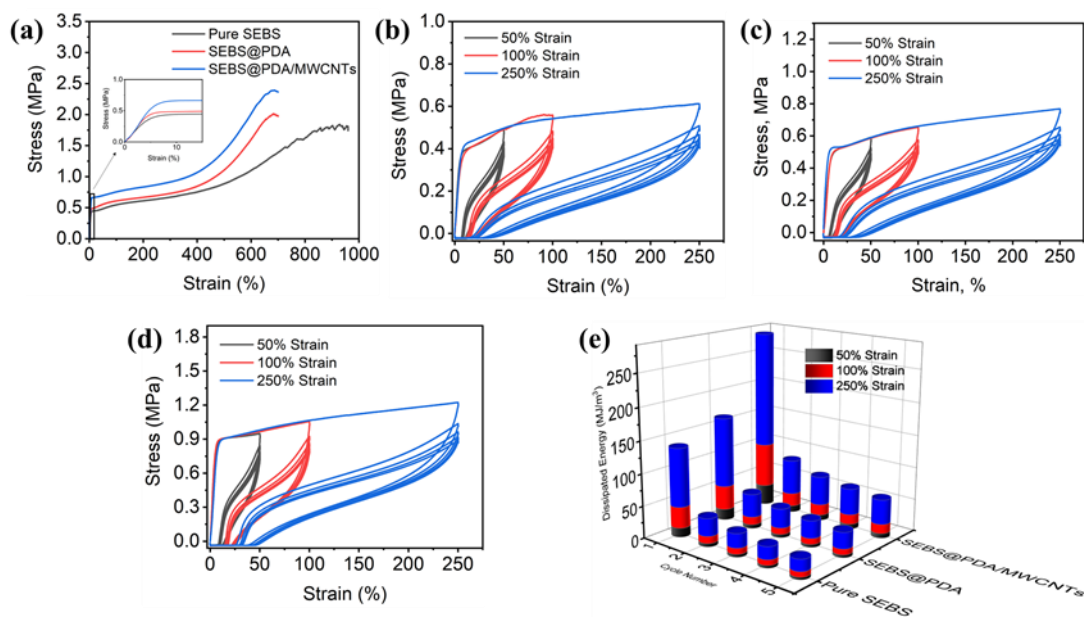


Figure 6 Stress–strain curves of pure SEBS, SEBS@PDA, and

SEBS@PDA/MWCNTs fibers at a stretching rate of 100 mm/min. Stress-strain curves of initial five tensile cycles of (b) pure SEBS fibers, (c) SEBS@PDA fibers, and (d) SEBS@PDA/MWCNTs fibers at different strains. (e) Dissipated energy of SEBS, SEBS@PDA and SEBS@PDA/MWCNTs fibers at different strains.

Table 1 Mechanical properties of Pure SEBS, SEBS@PDA, and SEBS@PDA/MWCNTs fibers: elastic modulus (E), tensile strength (σ) and elongation at break ($\epsilon_{at\ break}$)

	E (MPa)	σ (MPa)	$\epsilon_{at\ break}$ (%)
Pure SEBS	8.33 ± 0.36	1.84 ± 0.22	929.3 ± 100.04
SEBS@PDA	10.98 ± 0.68	2.01 ± 0.34	683.05 ± 86.24
SEBS@PDA/MWCNTs	11.67 ± 1.08	2.39 ± 0.62	626.92 ± 74.52

3.5 Electromechanical Properties and Modeling the Strain Sensing Mechanism

To determine the sensing behavior, the change of relative resistance for SEBS@PDA/MWCNTs fibers applied with a tensile speed of 10 mm/min is depicted in Figure 7. It can be seen from Figure 7a that SEBS@PDA/MWCNTs fibers had a wide workable strain range of 0 ~ 530%. Generally, it has usually been necessary to study the constriction strain sensing mechanism, constriction mechanism [37] and tunneling effect [3,29] to correlate laboratory results with values experienced in practical applications for the strain sensors.

Here, the tensile conductive mechanism of resistance change in the composite fibers was proposed as below, and Figure 7b and 7c illustrate the whole structural changes of

three stages during stretching. For the conductive fillers uniformly distributed in the flexible matrix, under low strain the uniformly distributed conductive fillers recombined which resulted in partial aggregation of conductive fillers, so a highly heterogeneous structure of conductive phase was formed. This nonuniformity led to a change of conductive path from wide to narrow and this constricted the current flow, resulting in an increase of resistance [37]. Thus, under a strain of 10%, a constriction mechanism can be used to explain the material conductive behavior. The change in resistance $\Delta R/R$ of the composites can be calculated using Equation 2 [37]:

$$\frac{\Delta R}{R_0} = \frac{R(\varepsilon) - R(\varepsilon_0)}{R(\varepsilon_0)} = \left[\left(\frac{\varepsilon_1 - \varepsilon_0}{\varepsilon_1 - \varepsilon} \right)^{1/2} - 1 \right] \times 100 \quad (2)$$

where $R(\varepsilon)$ and $R(\varepsilon_0)$ are the resistances at strains of ε and ε_0 , respectively. The units of relative resistance and strain are both %. ε_1 and ε_0 are the upper and lower limits of the strain range, which are 10% and 0% respectively.

It can be seen from Figure 7a that the experimental results in domain I are in good agreement with those calculated using Equation 2, indicating the effectiveness of the constriction mechanism in this strain range.

With the increasing strain, the conductive fillers were separated from each other. The electrons were transported mainly through the nanoscale gap between conductive fillers. The change of resistance was ascribed to one or both of two reasons. On the one hand, it was due to the change in number of conductive paths caused by the fracture of the conductive network. On the other hand, it was caused by the change of tunnel distance between conductive fillers. Therefore, the change of resistance in the next domain was in accordance with the tunneling effect proposed by Simmons [38]. The resistance (R)

of the composites can be calculated using Equation 3:

$$R = \left(\frac{L}{D}\right) \left(\frac{8\pi h s}{3\gamma a^2 e^2}\right) \exp(\gamma s) \quad (3)$$

where D and L represent the number of conductive paths and the number of particles forming a single path, h and e are Planck constant and electronic charge respectively, s is the minimum distance between conductive fillers, and a^2 is the effective cross-section. γ is a parameter representing the barrier height (ϕ) and a function of the electron mass (m), which is given by Equation 4.

$$\gamma = \frac{4\pi}{h} \sqrt{2\phi m} \quad (4)$$

Assuming that the initial distance (s_0) and the number of conductive paths (N_0) change to s and N under stress, their values are given by Equation 5 and 6, respectively

$$s = s_0(1 + b\varepsilon) \quad (5)$$

$$N = \frac{N_0}{\exp(A_1\varepsilon + B)} \quad (6)$$

where b , A_1 and B are constants. Therefore, the relationship between the change of resistance (ΔR) and strain is given by Equation 7.

$$\frac{\Delta R}{R_0} = \frac{R - R_0}{R_0} = \left(\frac{Ns}{N_0 s_0}\right) \exp[\gamma(s - s_0)] - 1 \quad (7)$$

By substituting Equations 5 and 6 into Equation 7, the relationship between relative resistance and strain is given by Equation 8.

$$\frac{\Delta R}{R_0} = \left(1 + \frac{\varepsilon}{100}\right) \exp\left(\frac{A\varepsilon}{100} + C\right) \times 100 \quad (8)$$

where the units of relative resistance and strain are both %, $A = A_1 + \gamma s$.

The relative resistance of composite fibers was calculated using Equation 8. As shown the curve of domain 2 of Figure 7a, good consistency between experimental and theoretical results was obtained in the strain range of 10% ~ 300%, where the fitting

constants A and B were determined to be 1.29 and 0.25, respectively.

With the increase in the strain beyond 300%, the increase of relative resistance was much more rapid than previous strain range. Although multiple fitting parameters were used in Equation 8, a consistency between experimental and theoretical results was not obtained in this domain. This may be due to considerable damage to the conductive network. Consequently, the number of conductive paths in the high strain range is given by Equation 9.

$$N = \frac{N_0}{\exp(E_1\varepsilon + F\varepsilon^2)} \quad (9)$$

where E_1 and F are constants. The relationship between relative resistance and strain is given by Equation 10.

$$\frac{\Delta R}{R_0} = \left(1 + \frac{\varepsilon}{100}\right) \exp\left[\frac{E\varepsilon}{100} + F\left(\frac{\varepsilon}{100}\right)^2\right] \times 100 \quad (10)$$

where the units of relative resistance and strain are both %, $E = E_1 + \gamma_s$.

As can be seen from Figure 7a, the model matched the experimental data reasonably well in the strain range of 300% ~ 530% with fitting constants of E and F are 1.63 and -0.07, respectively. Table 2 gives the relevant fitting equations and fitting constants used to model relative resistance in the three stages.

Table 2 Fitting equations and constants for the three stages presented in Figure 7a

Domain	Strain	Fitting equation	Fitting constant
I	0% ~ 10%	$\frac{\Delta R}{R_0} = \left[\frac{R(\varepsilon) - R(\varepsilon_0)}{R(\varepsilon_0)} \right. \\ = \left. \left(\frac{\varepsilon_1 - \varepsilon_0}{\varepsilon_1 - \varepsilon} \right)^{1/2} - 1 \right] \times 100$	—
II	10% ~	$\frac{\Delta R}{R_0} = \left(1 + \frac{\varepsilon}{100}\right) \exp\left(\frac{A\varepsilon}{100} + C\right) \times 100$	$A = 1.29$

	300%		$B = 0.25$
III	300% ~	$\frac{\Delta R}{R_0} = \left(1 + \frac{\varepsilon}{100}\right) \exp\left[\frac{E\varepsilon}{100}\right] + F \left(\frac{\varepsilon}{100}\right)^2] \times 100$	$E = 1.63$
	530%		$F = -0.07$

Figure 7d shows the GF of the SEBS@PDA/MWCNTs composite fibers, which is often used to evaluate the degree of sensitivity. As can be seen from the Figure 7d, GF increased with the increase in the strain. When the strain reached a maximum of 530%, GF was 3717. In Figure 7e, the maximum GF and workable strains were compared with strain sensors recently reported [6,10,12,14,17-19,39-50]. The comparison clearly demonstrated the exceptional comprehensive sensing performance of SEBS@PDA/MWCNTs composite fibers described in this work. Particularly, the developed composite fibers sensors simultaneously achieved a high workable strain range and a high GF.

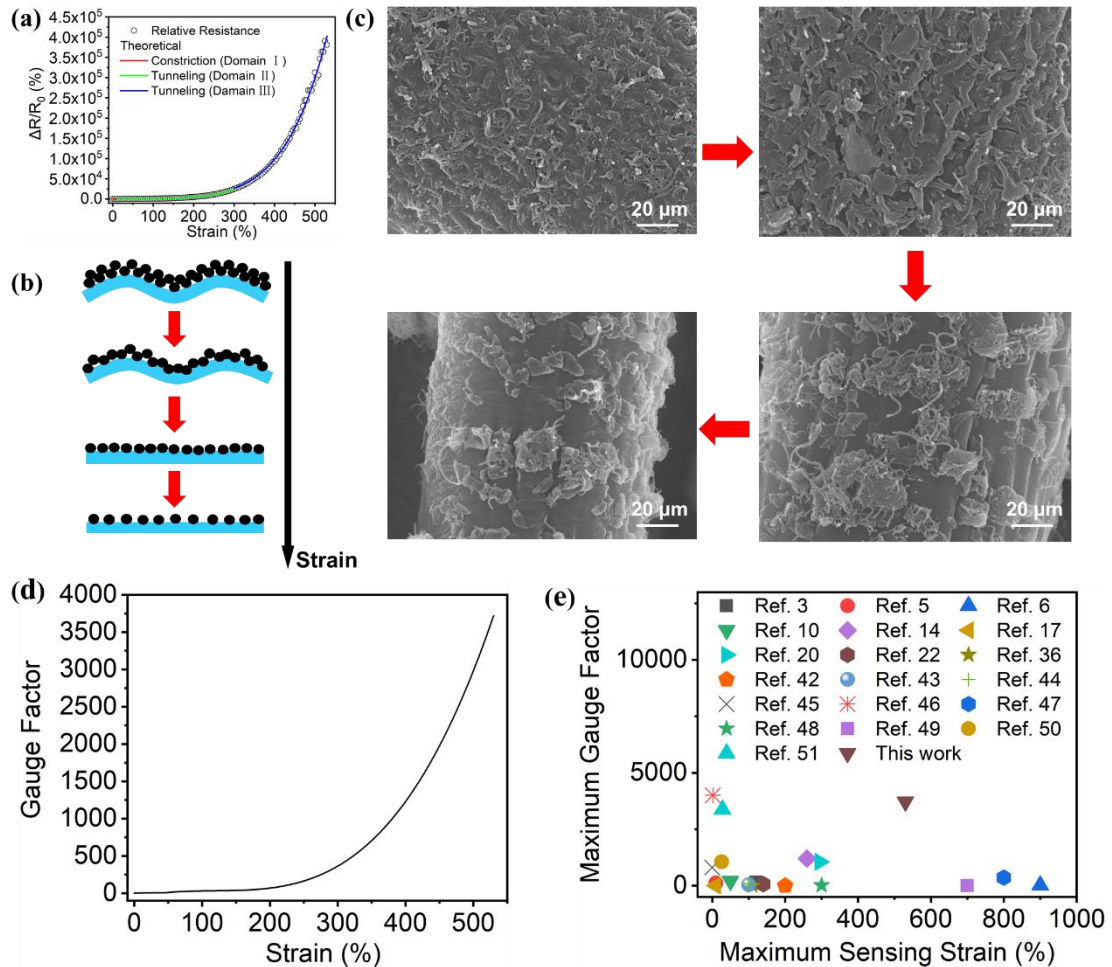


Figure 7 (a) The relative resistance–strain curve of fiber composites at a stretching rate of 10 mm/min. (b) The schematic illustration of longitudinal sections of fiber composites during stretching. (c) The SEM images of fiber surface during stretching. (d) The gauge factor–strain curve of fiber composites at a stretching rate of 10 mm/min. (e) Summary of reported values of the maximum GF and the maximum workable strain from the literature in the previous 4 years and results from this work.

To investigate the reliability and stability of composite fibers at different applied strains, the dynamic strain sensing behavior was determined from tensile cycles as shown in Figure 8a-c. As can be observed from Figure 8a and 10b, composite fibers exhibited excellent repeatability and stability in different strains at a frequency of 0.008 Hz and

a stretching rate of 10 mm/min respectively. Figure 8c shows the sensing behavior at different stretching rates and at a fixed strain of 100%. The similar changes in relative resistance can be seen under different stretching rates, revealing their ability to detect different external stimuli.

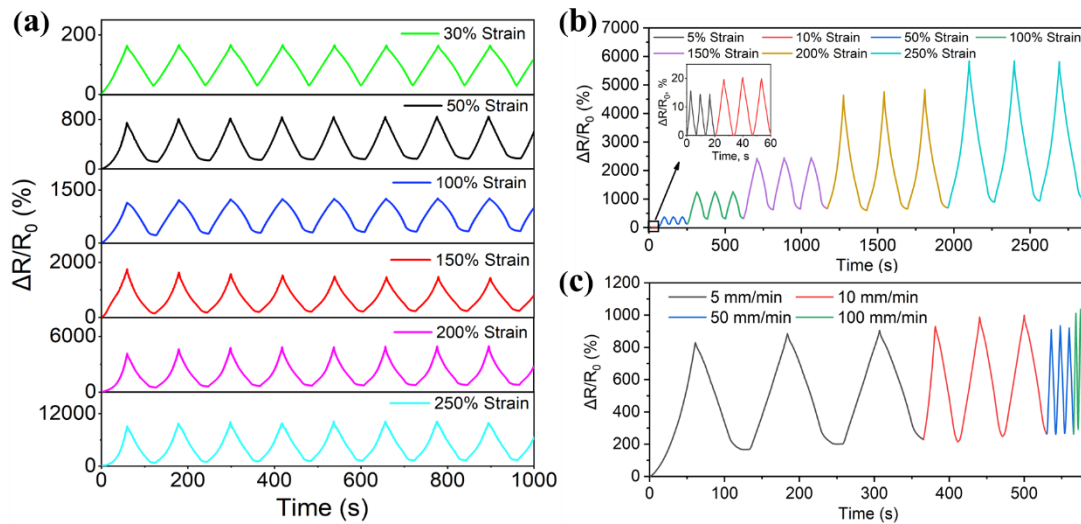


Figure 8 (a) The change of relative resistance of fiber composites under different strains of 30%, 50%, 100%, 150%, 200%, and 250% in tensile cycles at a frequency of 0.008 Hz. (b) The change of relative resistance of fiber composites under different strains of 5%, 10%, 50%, 100%, 150%, 200% and 250% in tensile cycling at a stretching rate 10 mm/min. (c) The change of relative resistance of fiber composites under different stretching rates of 5 mm/min, 10 mm/min, 50 mm/min, and 100 mm/min at a strain of 100%.

Figure 9a shows the current (I) and voltage (V) curves of composite fibers under different strains. The I-V curves under different strains show a linear relationship, indicating the compliance with Ohm's Law. Also, the long-term sensing behavior of the composite fibers was evaluated. In Figure 9b, at a strain of 40% and frequency of 0.25 Hz, the resistance increased initially and tended to stabilize after several tensile

cycles. This could be caused by the continuous destruction and reconstruction of conductive pathways, which helps stabilize the conductive networks at the commencement of tensile cycles [51]. Thereafter, the change in the resistance stabilized during 10000 s (2500 cycles), exhibiting good durability of the composite fibers.

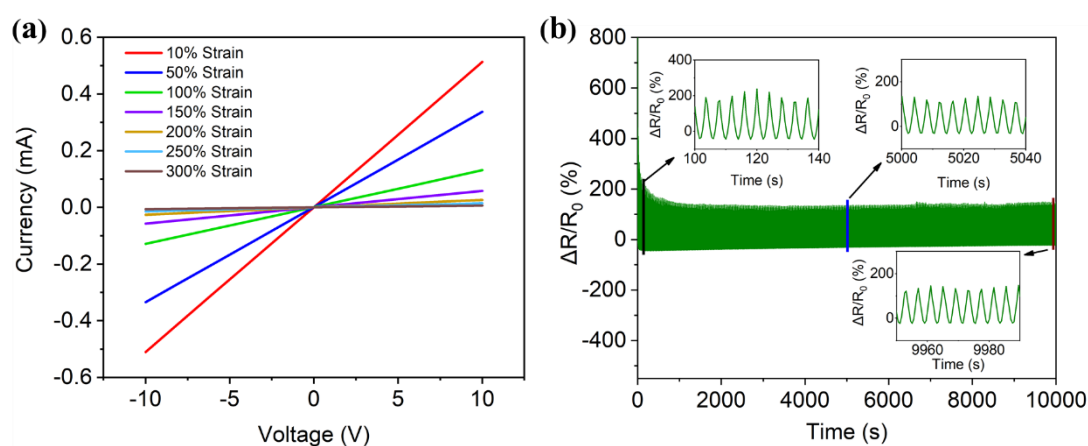


Figure 9 (a) Current and voltage of fiber composites under different strains of 10%, 50%, 100%, 150%, 200%, 250%, and 300%. (b) 2500 cycles at 0–40% strain at a frequency of 0.25 Hz.

3.6 Washing Fastness

To characterize the washing fastness, composite fibers were soaked in distilled water and ultrasonicated in a high-power ultrasonic cleaner for a range of time periods. As shown in Figure 10a, the sheet resistance of composite fibers changed from 1.34 k Ω /sq to 3.09 k Ω /sq after the first 40 min. After 120 min, the sheet resistance was still maintained to be 3.13 k Ω /sq. Meanwhile, its maximum workable strain can be up to 528%, which was comparable to the maximum workable strain before washing (530%) (Figure 10b). The composite fibers after washing it also exhibited good sensing behavior at a stretching rate of 10 mm/min and at a fixed strain of 100% (Figure 10c). This was due to the attraction between the ion on amide group on DA and polyanion

contained in carboxyl group, which enhanced the binding force between MWCNTs and PDA. It can be concluded that the composite fibers sensors had good washing fastness.

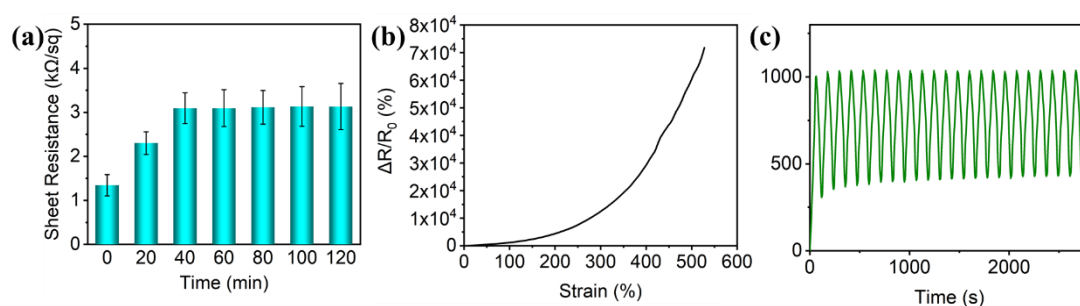


Figure 10 (a) The sheet resistance of fiber composite under different washing time. (b) The relative resistance–strain curve of fiber composites after washing at a stretching rate of 10 mm/min. (c) The change of relative resistance of fiber composites after washing under the strain of 100% in tensile cycling at a stretching rate 10 mm/min.

3.7 Human Motion Monitoring

As mentioned previously, the composite fibers had high flexibility, extensibility and durability. This meant they had potential applications in wearable strain sensors. The developed composite fibers were employed to monitor human motion to demonstrate their potential application in wearable strain sensors. As shown in Figure 11a, relatively resistance was recorded, indicating pulse beating were detected when composite fibers sensor was attached to the volunteer’s wrist. Informed consent was obtained from the volunteer before conducting the tests. Also, very pronounced changes in the relative resistance varied with the volunteer speaker’s pitch of voice (Figure 11b), showing the sensor’s ability to detect the voice-induced. Detection of other joint motions were also conducted using this sensor such as finger, elbow and knee joints bent through different angles. As shown in Figure 11c-e, relative resistance increased with the increasing joint

bend angle and decreased as the joint returns to its equilibrium position. These test results demonstrated that the developed composite fibers sensors can detect not only subtle strains (pulse beats and vocal cord vibration), but also large strains (finger, knee and elbow bending)

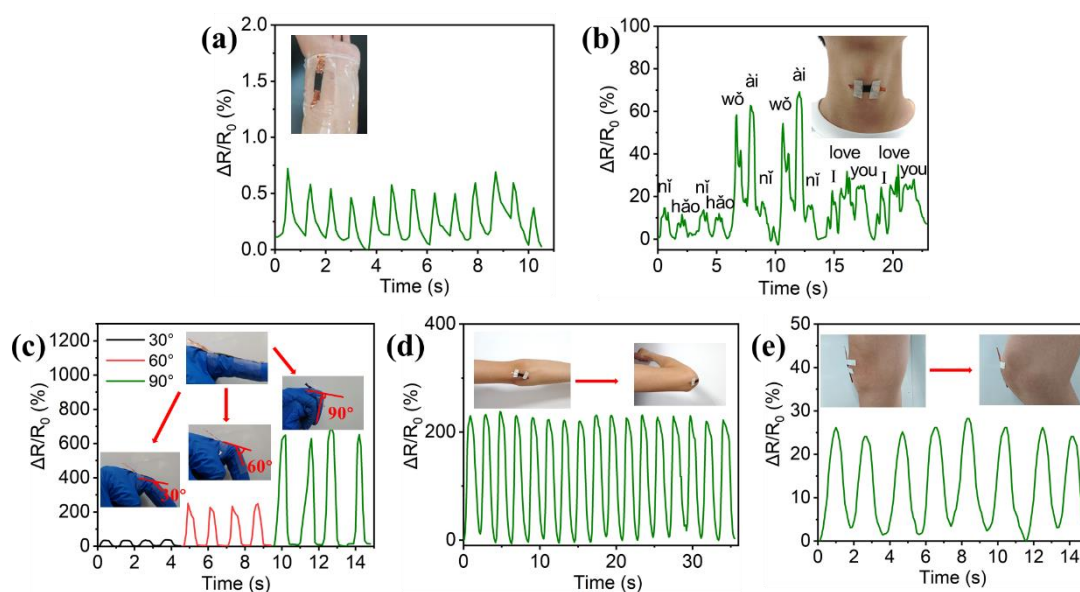


Figure 11 Strain sensors used to monitor human motions. (a) pulse beat, (b) vocal cord vibration, (c) finger bending, (d) elbow bending, (e) knee bending.

Conclusion

In this study, a new type of highly stretchable and sensitive strain sensor has been reported. This sensor was based on electrospun SEBS fibers coated sequentially by DA and MWCNTs-COOH under vacuum filtration. This fabrication method is simple and has low manufacturing costs. The fabricated strain sensor had a high GF of 3717 under a maximum workable strain of 530%. It also exhibited good durability and repeatability for different applied strains, different stretching rates and long-term cyclic loading. Furthermore, the sensor demonstrated excellent washing fastness under 120-min

ultrasonication, and superior performance in monitoring both subtle strains (pulse beat and vocal cord vibration) and large strains (finger, elbow and knee bending). These results have demonstrated that the developed strain sensor had a great potential as an excellent candidate for use in smart wearable devices.

Acknowledgements

The authors gratefully acknowledge the National Natural Science Foundation of China (Grant No. 51703108), the Shandong Provincial Key Research and Development Program, China (Grant No. 2019GGX102071), the Youth Innovation Science and Technology Plan of Shandong Province (2020KJA013) and the **Shandong “Taishan Youth Scholar Program”** (Grant No. tsqn201909100) for financial support.

Reference

1. C. Yan, J. Wang, W. Kang, M. Cui, X. Wang, C. Y. Foo, K. J. Chee, P. S. Lee. *Adv Mater.* **2014**, *26*, 2022-2027.
2. S. Hu, Z. Shi, W. Zhao, L. Wang, G. Yang. *Compos B Eng.* **2019**, *160*, 595-604.
3. X. Wang, S. Meng, M. Tebyetekerwa, Y. Li, J. Pionteck, B. Sun, Z. Qin, M. Zhu. *Compos Part A Appl Sci Manuf.* **2018**, *105*, 291-299.
4. L. Wang, Y. Chen, L. W. Lin, H. Wang, X. W. Huang, H. G. Xue, J. F. Gao. *Chem Eng J.* **2019**, *362*, 89-98.
5. Y. Chen, L. Wang, Z. F. Wu, J. C. Luo, B. Li, X. W. Huang, H. G. Xue, J. F. Gao. *Compos B Eng.* **2019**, *176*, 107358.
6. S. Shengbo, L. Lihua, J. Aoqun, D. Qianqian, J. Jianlong, Z. Qiang, Z. Wendong. *Nanot.* **2018**, *29*, 255202.
7. J. Wang, Y. Lou, B. Wang, Q. Sun, M. Zhou, X. Li. *Sens.* **2020**, *20*, 2459.
8. J. Huang, D. Li, M. Zhao, A. Mensah, P. Lv, X. Tian, F. Huang, H. Ke, Q. Wei. *Adv Electron Mater.* **2019**, *5*, 1900241.
9. J. Lee, S. Kim, J. Lee, D. Yang, B. C. Park, S. Ryu, I. Park. *Nanoscale.* **2014**, *6*, 11932-11939.
10. S. R. Pan, Z. Pei, Z. Jing, J. Q. Song, W. D. Zhang, Q. Zhang, S. B. Sang. *Rsc Advances.* **2020**, *10*, 11225-11232.
11. C. Lee, L. Jug, E. Meng. *ApPhL.* **2013**, *102*, 183511.
12. Y. H. Wang, W. Y. Li, Y. F. Zhou, L. Jiang, J. W. Ma, S. J. Chen, S. Jerrams, F. L. Zhou. *JMatS.* **2020**, *55*, 12592-12606.
13. W. Y. Li, Y. F. Zhou, Y. H. Wang, Y. Li, L. Jiang, J. W. Ma, S. J. Chen. *Macromol Mater Eng.* **2020**, *305*, 1900736.
14. Z. M. Shen, J. C. Feng. *J Mater Chem C.* **2019**, *7*, 9423-9429.
15. C. C. Jin, D. M. Liu, M. Li, Y. Wang. *J Mater Sci - Mater Electron.* **2020**, *31*, 4788-4796.
16. W. Son, K. B. Kim, S. Lee, G. Hyeon, K. G. Hwang, W. Park. *J Nanosci Nanotechnol.* **2019**, *19*, 6690-6695.
17. T. Lee, Y. W. Choi, G. Lee, P. V. Pikhitsa, D. Kang, S. M. Kim, M. Choi. *J Mater Chem C.* **2016**, *4*, 9947-9953.
18. Z. Wang, Y. Huang, J. Sun, Y. Huang, H. Hu, R. Jiang, W. Gai, G. Li, C. Zhi. *ACS Appl Mater Interfaces.* **2016**, *8*, 24837-24843.
19. M. Ren, Y. Zhou, Y. Wang, G. Zheng, K. Dai, C. Liu, C. Shen. *Chem Eng J.* **2019**, *360*, 762-777.
20. X. Li, K. Huang, X. Wang, H. Li, W. Shen, X. Zhou, J. Xu, X. Wang. *JMatS.* **2017**, *53*, 1191-1203.
21. S. Kuester, G. M. O. Barra, J. C. Ferreira, B. G. Soares, N. R. Demarquette. *Eur Polym J.* **2016**, *77*, 43-53.
22. M. Shin, J. Y. Oh, K. E. Byun, Y. J. Lee, B. Kim, H. K. Baik, J. J. Park, U. Jeong. *Adv Mater.* **2015**, *27*, 1255-1261.
23. J. Xu, S. Wang, G. N. Wang, C. Zhu, S. Luo, L. Jin, X. Gu, S. Chen, V. R. Feig, J. W. To, S. Rondeau-Gagne, J. Park, B. C. Schroeder, C. Lu, J. Y. Oh, Y. Wang, Y. H. Kim, H. Yan, R. Sinclair, D. Zhou, G. Xue, B. Murmann, C. Linder, W. Cai, J. B. Tok, J. W. Chung, Z. Bao. *Sci.* **2017**, *355*, 59-64.
24. P. L. Chuang, Y. H. Nien. *J Polym Res.* **2019**, *26*, 66.
25. W. Wei, H. Liang, K. Parvez, X. Zhuang, X. Feng, K. Mullen. *Angew Chem Int Ed Engl.* **2014**, *53*, 1570-1574.

26. G. S. Liu, X. Yan, F. F. Yan, F. X. Chen, L. Y. Hao, S. J. Chen, T. Lou, X. Ning, Y. Z. Long. *Nanoscale Res Lett.* **2018**, *13*, 309.
27. J. H. Ryu, P. B. Messersmith, H. Lee. *ACS Appl Mater Interfaces.* **2018**, *10*, 7523-7540.
28. C. H. Seager, G. E. Pike. *PhRvB.* **1974**, *10*, 1435-1446.
29. S. L. Yu, X. P. Wang, H. X. Xiang, L. P. Zhu, M. Tebyetekerwa, M. F. Zhu. *Carbon.* **2018**, *140*, 1-9.
30. M. Cai, H. He, X. Zhang, X. Yan, J. Li, F. Chen, D. Yuan, X. Ning. *Nanomater.* **2018**, *9*, 39.
31. Y. L. Zhao, S. G. Wang, Q. S. Guo, M. W. Shen, X. Y. Shi. *J Appl Polym Sci.* **2013**, *127*, 4825-4832.
32. J. X. Lin, W. W. Wang, J. Q. Cheng, Z. X. Cui, J. H. Si, Q. T. Wang, W. Z. Chen. *J Appl Polym Sci.* **2020**, *137*, 49252.
33. Z. Sang, K. Ke, I. Manas-Zloczower. *Compos Part A Appl Sci Manuf.* **2019**, *121*, 207-212.
34. S. Ribeiro, P. Costa, C. Ribeiro, V. Sencadas, G. Botelho, S. Lanceros-Méndez. *Compos B Eng.* **2014**, *67*, 30-38.
35. R. W. Ogden, D. G. Roxburgh. *Proc R Soc London, Ser A.* **1999**, *455*, 2861-2877.
36. N. Wang, Z. Xu, P. Zhan, K. Dai, G. Zheng, C. Liu, C. Shen. *J Mater Chem C.* **2017**, *5*, 4408-4418.
37. N. T. Selvan, S. B. Eshwaran, A. Das, K. W. Stöckelhuber, S. Wießner, P. Pötschke, G. B. Nando, A. I. Chervanyov, G. Heinrich. *Sensor Actuat a-Phys.* **2016**, *239*, 102-113.
38. J. G. Simmons. *JAP.* **1963**, *34*, 1793-1803.
39. P. Costa, S. Goncalves, H. Mora, S. A. C. Carabineiro, J. C. Viana, S. Lanceros-Mendez. *ACS Appl Mater Interfaces.* **2019**, *11*, 46286-46295.
40. B. X. Zhang, Z. L. Hou, W. Yan, Q. L. Zhao, K. T. Zhan. *Carbon.* **2017**, *125*, 199-206.
41. P. Costa, J. Oliveira, L. Horta-Romaris, M. J. Abad, J. A. Moreira, I. Zapirain, M. Aguado, S. Galvan, S. Lanceros-Mendez. *Composites Sci Technol.* **2018**, *168*, 353-362.
42. M. C. Zhang, C. Y. Wang, H. M. Wang, M. Q. Jian, X. Y. Hao, Y. Y. Zhang. *Adv Funct Mater.* **2017**, *27*, 1604795.
43. G. F. Yu, X. Yan, M. Yu, M. Y. Jia, W. Pan, X. X. He, W. P. Han, Z. M. Zhang, L. M. Yu, Y. Z. Long. *Nanoscale.* **2016**, *8*, 2944-2950.
44. S. Wang, X. Zhang, X. Wu, C. Lu. *Soft Matter.* **2016**, *12*, 845-852.
45. Y. Lin, S. Liu, S. Chen, Y. Wei, X. Dong, L. Liu. *J Mater Chem C.* **2016**, *4*, 6345-6352.
46. X. Liao, Z. Zhang, Q. Liao, Q. Liang, Y. Ou, M. Xu, M. Li, G. Zhang, Y. Zhang. *Nanoscale.* **2016**, *8*, 13025-13032.
47. C. G. Zhou, W. J. Sun, L. C. Jia, L. Xu, K. Dai, D. X. Yan, Z. M. Li. *ACS Appl Mater Interfaces.* **2019**, *11*, 37094-37102.
48. Y. J. Zheng, Y. L. Li, K. Dai, Y. Wang, G. Q. Zheng, C. T. Liu, C. Y. Shen. *Composites Sci Technol.* **2018**, *156*, 276-286.
49. X. Sun, Z. H. Qin, L. Ye, H. T. Zhang, Q. Y. Yu, X. J. Wu, J. J. Li, F. L. Yao. *Chem Eng J.* **2020**, *382*.
50. Y. F. Yang, L. Q. Tao, Y. Pang, H. Tian, Z. Y. Ju, X. M. Wu, Y. Yang, T. L. Ren. *Nanoscale.* **2018**, *10*, 11524-11530.
51. H. Liu, J. Gao, W. Huang, K. Dai, G. Zheng, C. Liu, C. Shen, X. Yan, J. Guo, Z. Guo. *Nanoscale.* **2016**, *8*, 12977-12989.